PCCP

Accepted Manuscript

ROYAL SOCIETY OF CHEMISTRY

www.rsc.org/pccp

PCCP

PAPER

Effect of particle size on electric and magnetic transport properties of $La_{0.67}Sr_{0.33}MnO_3$ coatings

Received 00th January 20xx,
Accepted 00th January 20xx

DOI: 10.1039/x0xx00000x

www.rsc.org/

Yu Zhou, Xinde Zhu and Shengli Li*

A systematic study of polycrystalline $La_{0.67}Sr_{0.33}MnO_3$ (LSMO) manganite coatings has been undertaken to analysis the effect of varying particle sizes on electromagnetic transport properties. In order to acquire a series of samples with different particle sizes, the samples were prepared by sol–gel method and were subjected to anneal at four different temperatures. With decreasing particle sizes, the magnetization decreases while the coercivity increases, which is attributed to the magnetically disordered surface layer. More attractively, the electrical transport properties can be systematically manipulated by particle sizes and so can the low field magnetoresistance (LFMR) values. Emphasis is placed on information that how the particle size affects the temperature dependence of resistivity and three conduction models are explored to describe the transport behaviours in three temperature regions. A minimum of resistivity is observed in the low temperature region in the presence and absence of a magnetic field, which can be mainly explained as the intergranular spin polarized tunneling (ISPT) through the grain boundaries (GBs) in polycrystallines.

1. Introduction

The hole-doped rare-earth perovskite manganites of the general formula $RE_{1-x}A_xMnO_3$ (RE=rare earth ion, A= Ca, Sr, Ba, Pb, *etc*., divalent alkaline earth metal ion), especially the doped lanthanum manganite $La_{1-x}Sr_xMnO_3$ (LSMO), have spurred considerable scientific and technological interest in the recent decades due to their remarkable electrical, magneto transport, catalytic and colossal magnetoresistance (CMR) properties, *etc*.[1-3] Conventionally, these properties of manganites can be explained by the theory of Zener's Mn^{3+}–O^{2-}–Mn^{4+} double-exchange (DE) effect,[4] a strong electron-phonon coupling arising from Jahn–Teller (J-T) splitting of the Mn d-level,[5, 6] orbital degree of freedom, and current carrier density collapse, *etc*. In the doped LSMO, on average, every La^{3+} substituted by a Sr^{2+} will result in a Mn^{3+} transferring into Mn^{4+} and when a third of Mn^{3+} transfers into Mn^{4+} (x~0.33), the system will reach the optimum transport state, which numerous reports have shown.[2, 7] The Mn^{3+}/Mn^{4+} ratio plays a particularly important role in governing the properties of manganites. A prominent feature of most manganites is that they will undergo a metal–insulator (M–I) transition at the temperature Tp accompanied by a ferromagnetic–paramagnetic (FM–PM) transition at the Curie temperature Tc (Tc≈Tp, Tp is generally a few degrees lower than Tc), which explains that there exists a close relation between the electrical and magnetic properties of the manganites.[5, 8] But Tc and Tp are close to only for manganites which have a ferromagnetic state with proper long-range order and small or intermediate band widths such as $Pr_{1-x}Ca_xMnO_3$ (PCMO) and $La_{1-x}Ca_xMnO_3$ (LCMO), and for the other manganites with large bandwidths like LSMO, Tc and Tp may differ by more than 100 K.[9-11]

CMR is caused by a magnetic field-induced enhancement of the carrier mobility and a suppression of the thermal magnetic disorder[2], while the carrier density is not affected.[12] The appealing potential application of the CMR materials is primarily in data storage field such as magnetoresistive read heads and magnetic random access memory, *etc*.[13, 14] Nevertheless, the practical application of the intrinsic CMR effect is limited by the following two essential external conditions: one is the temperature low enough or near Tc, and the other one is a large external magnetic field (several teslas).[7] To overcome this problem, a lot of researches have been conducted in the hope of acquiring high magnetoresistance (MR) values with low magnitude of applied magnetic field (H≤1T), i.e., low field magnetoresistance (LFMR).[2, 7] Experiments have suggested that the extrinsic nature of strong intergranular spin-polarized tunneling (ISPT)[15] of conduction electrons inside magnetic domains through the neighbouring grain boundaries (GBs) in polycrystallines contribute the most to the LFMR behaviour.[2, 11, 16-20] GBs act as centres of strong spin-dependent scattering of conduction electrons.[18, 21] The number of non-artificial GBs can be tuned by the difference of particle sizes, and thus the particle size effect is a key point affecting LFMR.[22] However, in order to elucidate the particle size effect on electromagnetic transport properties in polycrystalline manganites, more detailed studies are still in demand.

School of Materials Science and Engineering, Shandong University, Shandong Ji'nan, 250061, P. R. China *E-mail: lishengli@sdu.edu.cn*

†Electronic Supplementary Information (ESI) available: See DOI: 10.1039/x0xx00000x

Herein, we explore the possibility of particle size control using the sol-gel method and annealing process at different temperatures rather than using sophisticated artificial devices for the preparation of polycrystalline $La_{0.67}Sr_{0.33}MnO_3$ coatings. Sol-gel method is an important technique generally for preparing perovskite oxides because of short reaction time, the stabilized, homogeneous and high surface area of products, *etc*. Since the Mn^{3+}/Mn^{4+} ratio of manganites does not depend much on the particle sizes,[21] the effect of the Mn^{3+}/Mn^{4+} ratio on the property differences of the samples with different particle sizes is eliminated.

In this work, our principal objective is to systematically investigate the influence of particle size on the structure, electrical, magnetic and MR properties and assess the underlying mechanisms of these properties in micro-sized and nano-sized manganites.

2. Experiment section

The LSMO powders were prepared by the standard Pechini sol-gel method by using metal nitrate salts ($La(NO_3)_3.6H_2O$, $Sr(NO_3)_2$ and 50% $Mn(NO_3)_2$ solution) as precursors, citric acid ($C_6H_8O_7{\cdot}H_2O$) as chelating agent, ethylene glycol ($(CH_2OH)_2$) as surfactant to prevent the colloidal particles from aggregation, and deionized water as solvents. The stoichiometric molar ratio of La: Sr: Mn: O was controlled at 0.67:0.33:1:3. Each metal nitrate aqueous solution was separately heated to 65°C for 10 min with a mechanical stirrer to dissolve completely, mixed with $C_6H_8O_7{\cdot}H_2O$ and $(CH_2OH)_2$ in the molar proportion of 1:1.2:4.8, and then heated to 65°C for 20 min to remove water. Subsequently, all the solutions were mixed together under constant stirring for 6 h at 75°C and then maintained at 40–50°C for about 1 h to obtain a clear, homogeneous and viscous gel. The wet gel was put in the drying oven for more than 24 h to dry intensively, and then the dry gel was calcined in a furnace at 800°C for 2 h to form LSMO powders. According to our previous work,[23] TG/DSC curves for the LSMO gel precursor have been carried out which showed that there was basically no weight loss around 800°C, and the highest crystallinity with the smallest size possibly was obtained at 750 °C,[2, 24] so we chose the temperature of 800°C as the calcining temperature.

To prepare the LSMO coatings on Al_2O_3 substrates, the screen-printing method was employed. Before coating, the substrates were pre-treated in nitric acid for 3 min, in sodium hydroxide for 3 min and in distilled water for 3 min to clean up (each step was accompanied by an ultrasonic cleaning process). The coating slurry comprised of 68 wt% alpha-terpineol as organic solvent, 2 wt% ethyl cellulose ($(C_6H_{10}O_5)n$) as thickening agent and 30 wt% of grinded LSMO powders as functional material was screen printed directly onto substrates by a screen plate of 120 mesh. This cycle was repeated in order to obtain coatings with a final thickness of around 50 µm. Then the wet coatings went through a series of procedures of flowing and drying, followed by the process of annealing in air atmosphere at 900°C, 1000°C, 1100°C and 1200°C for 2 h, named as sample LSMO-9, LSMO-10, LSMO-11 and LSMO-12, respectively.

The thickness, particle size, morphology, and element distribution of the LSMO coatings were evaluated by field emission scanning electron microscopy (FESEM, SU-70, Hitachi) equipped with energy dispersive spectrometer (EDS). High-resolution transmission electron microscopy (HR-TEM) images and selected area electron diffraction (SAED) patterns were performed using a TEM (JEM-2100) operating at 200 kV. X-ray diffraction (XRD) patterns were collected on a Rigaku D/Max X-ray diffractometer with Cu Kα radiation (λ=1.5418Å) in a 2θ range of 20–70° at a scanning rate of 2 °min^{-1}. The crystal structure parameters of the samples were elucidated from the analysis of XRD patterns using Rietveld refinement with the MDI Jade software. The magnetic, electrical and MR properties were measured with a vibrating sample magnetometer (VSM, JDAW-2000D) at 300 K with applied fields of 0–9000 Oe and a Superconducting Quantum Interference Device (SQUID, MPMSXL, Quantum Design, USA) using the conventional four-point technique in the temperature range of 5–360 K under a magnetic field of 0-1 T. The LSMO samples mounted on MPMS sample stuck was placed parallel to the direction of the magnetic field.

3. Results and discussion

3.1 Structure and Morphology

Fig. 1 (a) shows the dense and crack-free surface morphology of the representative LSMO-12 coating. All the samples annealed at different temperatures are in the same batch of the screen-printing process and the thicknesses of the samples are basically analogous, so that the influence of the thickness difference on the properties is negligible. Fig.1 (b) presents the cross-section image of the representative LSMO-12 coating with the thicknesses of ~50 µm.

The grains of sample LSMO-9, LSMO-10, LSMO-11 and LSMO-12 have excellent crystallinity, and show agglomerated ellipsoidal shapes with average particle sizes of ~65nm, 80 nm, 300 nm, 730 nm, respectively. It is illustrated that with increasing the annealing temperature, the particle size of samples increases (Fig. 1 (c), (d) and Table 1). The special stepped morphology of the submicron particles of sample LSMO-11 and LSMO-12 indicates the tendency of growth and coalescence of particles from the core toward the surface of particles, which Anustup *et al*.[2] have also found.

The detailed morphology and structure of a single crystal and stacked ones of sample LSMO-12 were further characterized by TEM, as shown in Fig. 1 (e)-(g). The magnitude of the particle size of sample LSMO-12 is in good agreement with SEM results. The single crystal structure indentified by the SAED pattern (Fig. 1 (f)) reveals a typical electron diffraction pattern of the $[2\bar{2}1]$ zone of the rhombohedral LSMO structure. The interplanar spacing of (110) is 0.275 nm and that of (012) is 0.388 nm. The HRTEM image of the region marked by the red box (in Fig. 1 (e)) and the corresponding FFT pattern are presented in Fig. 1 (g), which

Table 1. Experimental data of LSMO samples

		LSMO-9	LSMO-10	LSMO-11	LSMO-12
Annealing temperature (°C)		900	1000	1100	1200
Average particle size (nm)		65	80	300	730
Structure type		Rhombohedral	Rhombohedral	Rhombohedral	Rhombohedral
Space group		R$\bar{3}$c (167)	R$\bar{3}$c (167)	R$\bar{3}$c (167)	R$\bar{3}$c (167)
Lattice parameters	a=b (Å)	5.4935	5.4941	5.4973	5.5019
	c (Å)	13.3669	13.3697	13.3759	13.3782
	Volume (Å^3)	349.35	349.50	350.07	350.71
T_C (K)		335	340	342	345
$\Delta T=T_C-Tp$ (K)		195	150	72	---
T_{min} (K)	0 T	40	38	25	21
	1 T	39	31	16	12
Tp (K)	0 T	140	190	270	>300
	1 T	142	193	271	>300
MR at 1T (%)	5 K	22.56	21.88	21.63	16.54
	300 K	4.57	4.29	2.36	1.30

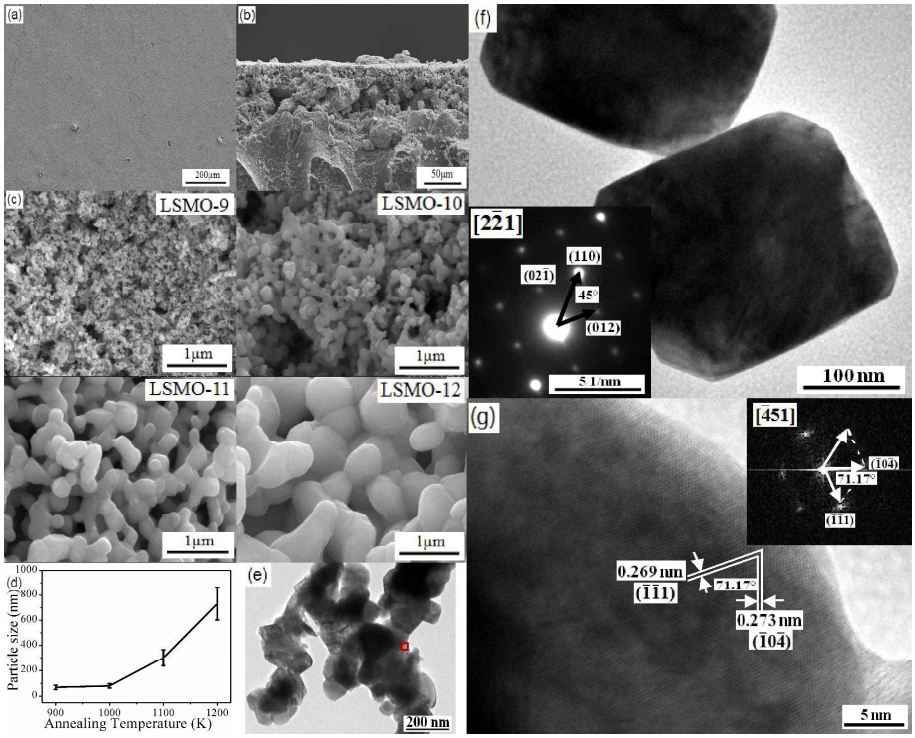

Fig. 1 (a) The surface morphology of sample LSMO-12, (b) the cross-section morphology of sample LSMO-12, (c) the grain morphology of the samples, (d) annealing temperature dependence of particle size of the samples, (e) the TEM image of sample LSMO-12, (f) the TEM image and SAED image (the inset) of a single crystal of sample LSMO-12, (f) the HRTEM image of the region marked by the red box (in (e)) of sample LSMO-12, the upper inset is the corresponding FFT pattern.

illustrates that the complete structure of the region is an interconnected grain and the two crystal grains are oriented by an angle of 71.17°. The interplanar spacing is calculated to be about 0.269 nm and 0.273 nm, respectively, which are coincident with the ($\bar{1}\bar{1}$1) and (10$\bar{4}$) crystal planes of the rhombohedral LSMO structure.

The compositional homogeneity of sample LSMO-12 was checked by the EDS analysis (Fig. S1). It is shown the evenly distribution of all the elements and the La: Sr: Mn: O atomic ratio is about 0.64:0.36:1:3.10 which basically matches with the starting ratio of 0.67:0.33:1:3. Considering the test errors and the errors during experiment operation, the result showsthat the sol-gel method insures the composition homogeneity and is suitable for the fabrication of LSMO samples.

XRD patterns of the LSMO coatings are shown in Fig 2 and the Rietveld refined unit cell parameters are listed in Table 1. In view of the incomplete flatness of the coatings and the experimental errors, the slight difference of the thickness of the coatings leads to the difference in ray transmittance, thus the basal scattering intensity of the samples may not be consistent. Results for all the coatings show single-phase rhombohedral crystal structure with R$\bar{3}$c space group and no impurities are detected. It also can be seen that most of the

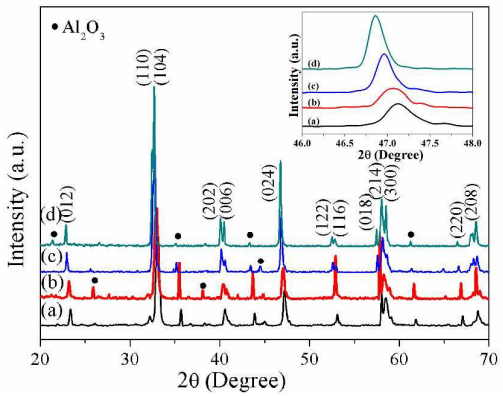

Fig. 2 XRD patterns of the LSMO samples (a) LSMO-9, (b) LSMO-10, (c) LSMO-11, (d) LSMO-12. The inset shows the peak profile at 2θ≈47^0 width of the diffraction peak (024) of the samples.

peaks are sharp and high, which reveals that the samples crystallized perfectly. It also indicates that all the coatings have no preferred orientations attributed to that the diffraction peak relative intensity ratios of LSMO coatings show similarity to the diffraction patterns of LSMO powders reported previously.[25, 26] With increasing particle sizes, the peaks shift towards lower angle side and narrow down, and peak intensity increases, accompanied by the increasing of the cell parameters and cell volume (inset of Fig. 2 and Table 1), which can be interpreted in a way that as the particle size increases, the lattice expands from nanometre to micrometre size, the inter-planar spacing increases, and thus the peaks shift towards lower angle side. These behaviours are also in accord with the results reported earlier.[3, 13, 27, 28] Zhang *et al.*[29] proved the structural distortion slightly increases with decreasing particle sizes.

3.2 Magnetic Properties

To get further insight into the source of the magnetic behaviour of polycrystalline samples with different particle sizes, we have carried out magnetic property measurements of the applied magnetic field (H) dependence of magnetization (M) at 300 K. Note that the magnetization for all samples does not reach saturation in the applied magnetic fields up to 9 kOe and the hysteresis loop is small without noticeable remanence (Mr) and coercivity (H_C) (as shown in Figure 3), which serve as clear evidences of the weak ferromagnetic state and multiphase (ferromagnetic and paramagnetic) nature of the test magnetic system. Zhang *et al.*[29] also confirmed that with the reduction of particle sizes, the manganites may have a multidomain structure of the particle size of >25 nm.

For better understanding of the magnetic behaviours, we have also applied the plotted well-known Arrott-Belov-Kouvel (ABK) plot (M^2 versus H/M) of the samples, as shown in lower insets of Fig. 3. The Arrott plots show a strong convex curvature and a finite spontaneous magnetization (Msp), which proves the existing of ferromagnetic phase of the samples.[13, 30] The Msp value can be estimated by the linear fitting of the high magnetic field part of the ABK plot and the M^2-intercept. The calculated Msp values are 3.20, 7.80, 14.38 and 22.45 emu/g of the sample LSMO-9, LSMO-10, LSMO-11 and LSMO-12, respectively. As the particle size decreases, the Msp and the curvature values decrease, which is probably attributed to the increase in the GB pinning centre of the grains and random canting of the particle surface spins caused by competing antiferromagnetic exchange interactions at

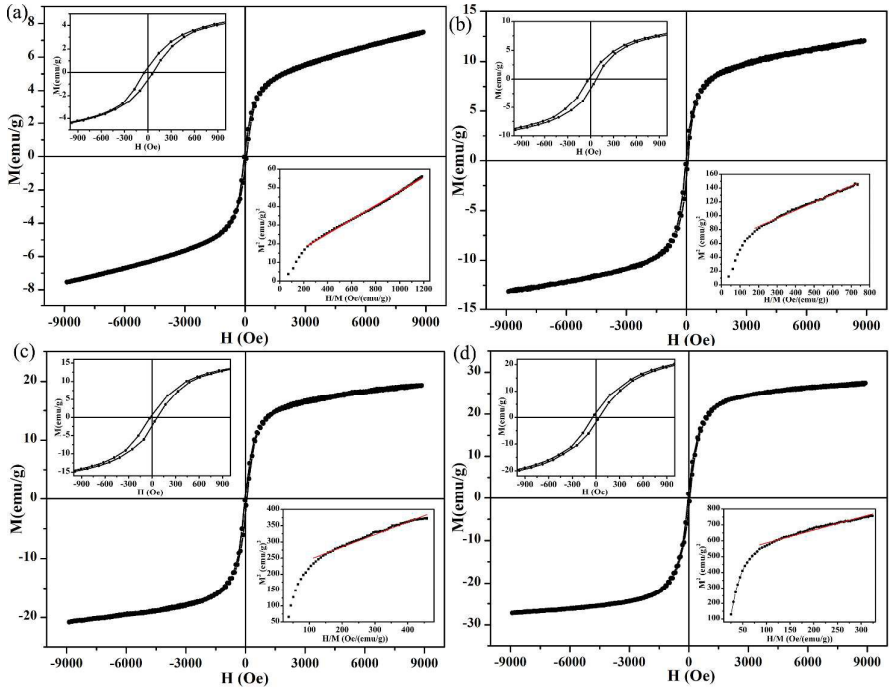

Fig.3 The M-H plots of the samples at 300 K, the upper insets show enlarged view of the M–H loop, the lower insets show ABK plots of the samples (a) LSMO-9, (b) LSMO-10, (c) LSMO-11, (d) LSMO-12.

the surfaces,[30, 31] and thus leads to the decrease of the ferromagnetic order and a weaker ferromagnetic state.[13]

The Mr values are 1.80, 1.05, 0.97 and 0.37 emu/g, and the Hc values are 49.53, 40.84, 35.77 and 24.82 Oe of the sample LSMO-9, LSMO-10, LSMO-11 and LSMO-12, respectively. The values of Hc and Mr of the LSMO samples display similar behaviour and both parameters increase progressively, while the values of magnetization decrease with the decrease of particle sizes. The additional surface magnetic anisotropy sourced from a magnetically disordered surface layer called dead or passivating layer of 2-5 nm with dangling or broken bonds that present in nanoparticles is usually the evidence of the phenomenon.[2, 13, 32-35] The layer is largely antiferromagnetic and amorphous in nature which has a random and chaotic orientation of spins, and the coupling among the magnetic ions in the surface is weaker compared to that in ferrimagnetically aligned core spins.[32] With decreasing particle sizes, the thickness of passivating layer and the number of disordered spins increase, which are adverse to the ferromagnetic order, thus leads to the reduction of magnetization and the increase of Hc and Mr.[29]

Studies on the variation of magnetization with temperature were carried out in a temperature range of 5-360K under a magnetic field of 1 T (as shown in Fig. 4). During the test temperature range, the FM–PM transition occurs and the transition temperature Tc is defined as the maximum of the absolute value of the first derivative of the magnetization curve, i.e., dM/dT (as given in Table 1). With a reduction in particle sizes, the values of magnetization lower over the whole temperature range, the FM-PM transition becomes broad/gradual and the values of Tc slightly decrease. These

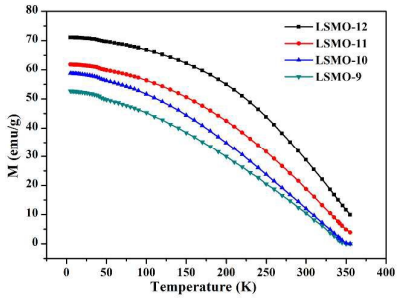

Fig. 4 Temperature dependence of magnetization of the LSMO samples under a magnetic field of 1 T.

observations suggest the magnetic inhomogeneity owing to the increasing of rhombohedral distortion and the narrowing of the bandwidth with the reduction of particle sizes, which also confirms similar results reported earlier.[9, 29]

3.3 Electrical properties

Since the electrical transport properties are closely related to magnetic properties of the LSMO samples and the magnetic properties are shown to be markedly affected by particle sizes, it is necessary to study the particles size effect on resistivity. The temperature dependent resistivity data in the range from 5 K to 300 K both in the presence and absence of a magnetic field (as shown in Fig. 5) can provide useful information of charge transport on the low temperature region (5 K<T<50 K), ferromagnetic metallic region (50 K<T<Tp) and paramagnetic insulating region (Tp<T<300 K) by fitting through three main conduction mechanisms.

3.3.1 Low temperature region (5 K<T<50 K)

In the low temperature region (5 K<T<50 K), with the decrease

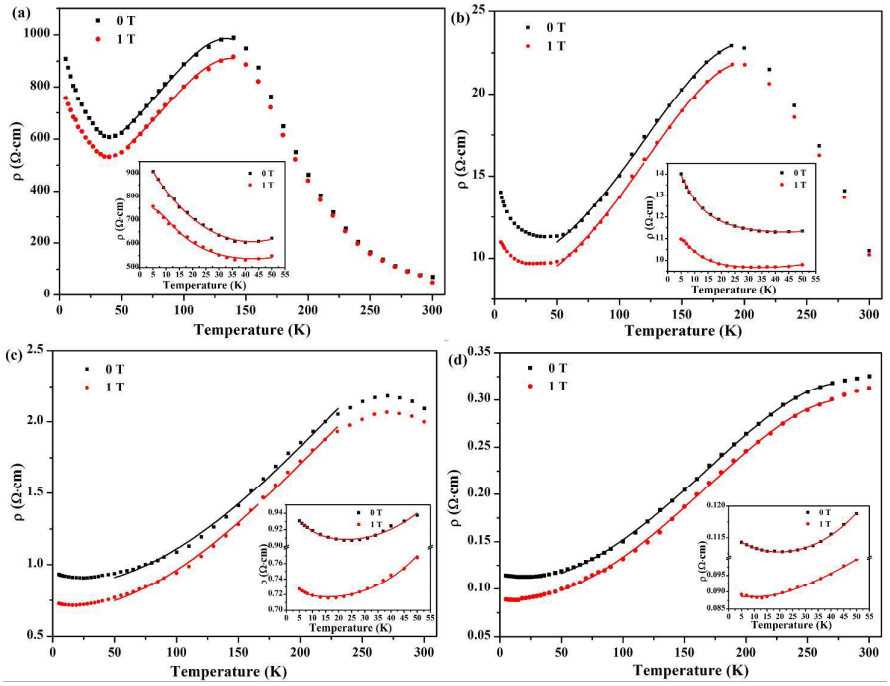

Fig.5 Temperature dependence of the resistivity of the LSMO samples at zero field and 1T, the insets are the fitting curves of resistivity at low temperature region (5 K<T<50 K) according to the ISPT model (a) LSMO-9, (b) LSMO-10, (c) LSMO-11, (d) LSMO-12.

of temperature, the resistivity of all the samples falls rapidly at first, subsequently, shows an anomaly of a minimum (T_{min}) at ~30 K, and then increases again, which exhibits a metal-semiconductor/insulating transition-like behaviour (Fig. 5). The depth of the minimum decreases substantially and T_{min} clearly shifts towards lower temperatures as the particle size increases, which can be presumably ascribed to the reduction of GB effect.[22] In addition, T_{min} shifts to a lower temperature and flattens out with applying a magnetic field of 1 T. The similar phenomenon also occurs in $Pr_{1/2}Sr_{1/2}MnO_3$,[36] $La_{1-x}Ag_xMnO_3$,[37] $La_{1/2}Ca_{1/2}MnO_3$,[38] *etc*., around 25 K.

Numerous models have been proposed to explain the field dependent resistivity minimum in low temperature region of granular materials.[1] In general, the origin of this phenomenon has been attributed to the competition of two contributions.[39] One is the Coulomb blockade effect (CB, an electrostatic blockade of carriers between grains)[1, 34, 40-42] of weak localization and strong electron-electron interaction with a disordered metallic state, based on which, the observed resistivity minimum can be expressed as:[43]

$$\rho(T)=\mathrm{A}\exp\left(E_c/T\right)^{1/2} \quad (1)$$

where E_c is the charging energy barrier (Coulomb barrier) that adds to the magnetic tunnel barrier which the localized charge carriers need to tunnel from grains to grains.[44] With the reduction of particle sizes, the contribution of Coulomb barrier increases, which in turn leads to a steeper rise in resistivity.

The other one is the intergranular spin-polarized tunneling (ISPT) model between antiferromagnetically coupled grains through the GBs proposed by Helman and Ables,[15] which is very sensitive to the applied field.[37] The antiferromagnetic interaction between the neighbouring grains with opposite and blocked spins causes an energy barrier under zero external field, and the spins get aligned to reduce the energy barrier with the application of external magnetic field, which can account for the flattening of resistivity minimum under some critical field.[37] In a simplified form, the resistivity minimum considering tunnelling through the GBs can be expressed as:[45]

$$\rho(T,H)=\frac{r_1+r_2T^{3/2}}{1+\varepsilon\left\langle\cos\theta_{ij}\right\rangle} \quad (2)$$

where r_1 and r_2 are field independent parameters of the grain *i* and *j*, respectively, $\varepsilon=P^2$ is spin valve coefficient and *P* is the degree of spin polarization of the charge carriers in each grain, $\cos\theta_{ij}$ is the angle between the magnetization directions n_i and n_j,[37] and the spin correlation function $\langle\cos\theta_{ij}\rangle$ for H=0 is represented by the following equation:

$$\left\langle\cos\theta_{ij}\right\rangle=-L\left(\frac{|J|}{k_BT}\right) \quad (3)$$

here, L(x)=coth(x)-1/x is the Langevin function and *J* is the inter grain antiferromagnetic exchange integral.[1]

In the presence of an external magnetic field (H≠0), Ciftja *et al*.[46] derived the analytical expression for spin correlation function $\langle\cos\theta_{ij}\rangle$, which is given by the following equation:

$$\left\langle\cos\theta_{ij}\right\rangle=\frac{1}{4}-\frac{1}{3+\exp\left(\frac{-3J_S}{k_BT}\right)} \quad (4)$$

here $J=S(S+1)J_S$ and *S* is the atomic ion spins.[1]

We have attempted to analyse our data based on the two models, and found that the ISPT model of field dependent[39, 45] provides a fairly well description of the effects observed (the fitting curves are shown in Fig. 5 insets and the fitting parameters of field and particle size dependent are shown in Table S1), while the first model of field independent[37, 39, 47] is not adequate for describing such behaviours. In addition, Das *et al*.[1] suggested that in general, the first model is observed for a very small grain size. Therefore, we can draw a conclusion that the ISPT model is primarily responsible for the resistivity minimum at low temperature of strongly field and particle size dependent of the polycrystalline manganites with larger particle sizes.

3.3.2 Ferromagnetic metallic region (50 K<T<Tp)

In this ferromagnetic metallic region, there is a ferromagnetically coupled interaction of electrons from neighbouring Mn^{3+} ($t_{2g}^3e_g^1$: S = 2) to Mn^{4+} ($t_{2g}^3e_g^0$:S = 3/2) ions through oxygen when their localized spins are parallel,[9] which is responsible for the simultaneous occurrence of ferromagnetism and metallic conduction below Tp in these manganites.[48]

The LSMO coatings show the M-I transition around the temperature range of 200K-300K, except the sample LSMO-12 whose Tp is above 300 K. With decreasing particle sizes, the resistivity of the samples increases, the value of Tp shifts to lower temperatures successively and ΔT=Tc-Tp goes up. These behaviours are presumably ascribed to that when the particle size decreases, the insulating and magnetically disordered layer is created around the grains (as previously mentioned),[3, 34] more localized electrons assemble near the surface, and the number of GBs is larger which act as barriers to the carriers.[2]

When a magnetic field is applied, the resistivity decreases greatly, which is known as the CMR effect[49] and Tp is found to shift towards higher temperatures. This may be due to the fact that the applied magnetic field induces more number of spins of Mn ions to get aligned, the conduction electrons (e_g) to transfer more easily between the neighbouring pairs of Mn^{3+} and Mn^{4+} ions via oxygen, and the paramagnetic insulating state to be suppressed.[50] Jakob *et al.*[51] and Singh *et al.*[52] also ascribed these behaviours to the applied external field which leads to an increase of spin ordering and a reduction of carrier localization.

In order to understand the conduction mechanism of the materials at this temperature region (50 K<T<Tp), the experimental data match well with an empirical equation of the type $\rho=\rho_0+\rho_nT^n$ as shown in the followings:[10, 21, 53]

$$\rho=\rho_0+\rho_2T^2 \quad (5)$$

$$\rho=\rho_0+\rho_{2.5}T^{2.5} \quad (6)$$

$$\rho(T)=\rho_0+\rho_2T^2+\rho_{4.5}T^{4.5} \quad (7)$$

where ρ_0, ρ_2T^2, $\rho_{2.5}T^{2.5}$, $\rho_{4.5}T^{4.5}$ represent the GB effect, the electron-electron scattering process, the single magnon scattering or electron-phonon scattering process, two magnon scattering or electron-magnon scattering process in the ferromagnetic region, respectively.[50, 54]

We can see from the experimental results that the resistivity data of the ferromagnetic and metallic part (50 K < T

< Tp) of the LSMO samples more favourably fits with the Eq. (7) which is in agreement with the experimental data up to 99% (as shown in Fig. 5 and Table S2). Kumari *et al.*[50] also approved that Eq. (7) is more appropriate than the other two to explain the intrinsic conduction mechanism in manganites. The fitting parameters are found to depend both on the particle size and the applied magnetic field.

3.3.3 Paramagnetic insulating region (Tp <T<300 K)

The resistivity decreases exponentially with the increase of temperature above Tp. The conduction behaviour in paramagnetic insulating region (Tp<T<Θ_D/2, Θ_D is Debye temperature, and the temperature at which deviation from linearity occurs is defined as the value of Θ_D/2 here[21]) both in the applied magnetic field of 0 T and 1 T may be explained by variable range hopping (VRH) mechanism which is typically found when conduction takes place by hopping between localized states:[55]

$$\sigma=\sigma_0 \exp(-T_0/T)^{1/4} \quad (8)$$

where $T_0=16\alpha^3/k_BN(E_F)$, and $N(E_F)$ is the density of states at the Fermi level, α=2.22 nm^{-1}.[21, 50] The curves of ln σ versus $T^{-1/4}$ have been plotted (as seen in Fig. 6), which indicate that ln σ of the samples shows linear dependence with $T^{-1/4}$ (Tp<T<300 K). The variation of relevant parameters (given in Table S3) is in excellent agreement with the reports of other researchers.[21]

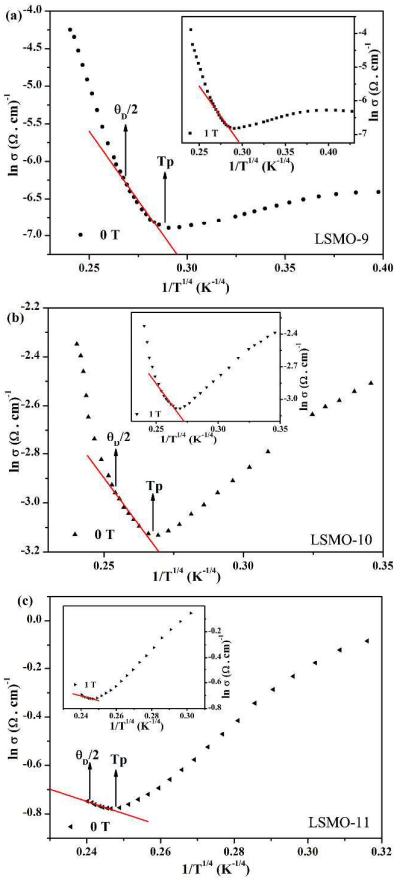

Fig. 6 Plots of ln σ versus $T^{-1/4}$ for the samples both in the presence and absence of a magnetic field according to the VRH model.

The T_0 values increase while N (E_F) values decrease with decreasing particle sizes both for 0 T and 1 T, which Fontcuberta *et al.*[55] have proved that the higher T_0 values of lower particle sizes associates with an increase of lattice distortion, a decrease of bandwidth and carrier mobility. For a particular particle size, T_0 value decreases while N (E_F) increases with the application of magnetic field, which is on account of the suppression of the magnetic domain scattering,[21] and the increase of the number of charges at the Fermi level.[50, 56]

3.4 Magnetoresistance Properties

Fig. 7 shows the temperature dependence of the MR % values at H=1 T of the LSMO samples. The MR % is defined as (ρ_0-ρ_H)/ρ_0 × 100, where ρ_0 and ρ_H are the resistivity with and without an applied magnetic field, respectively. Fig.8 shows the magnetic field dependence of the normalized resistivity (ρ_H/ρ_0) of the LSMO samples.

It is seen that in the temperature range of 5-300K, the values of MR increases monotonically as temperature decreases of the LSMO polycrystalline samples, which many other researchers[9, 11] also found. Generally speaking, the LSMO manganite system with large bandwidth exhibits higher MR

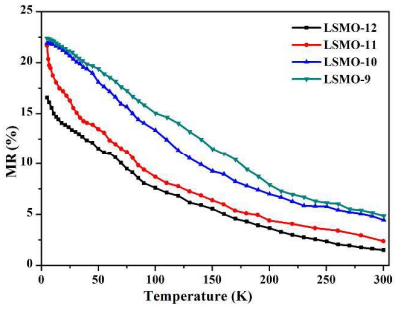

Fig.7 Temperature dependence of the MR values at H=1 T of the LSMO samples.

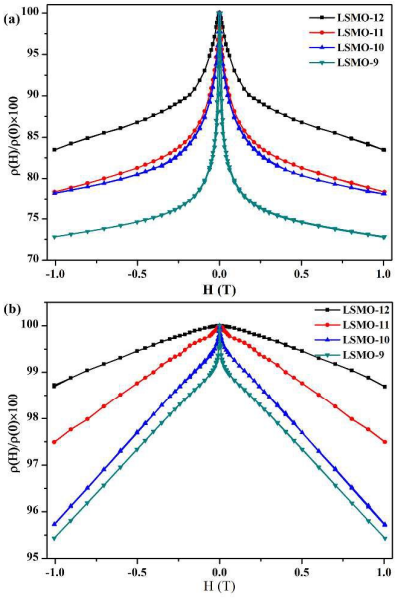

Fig. 8 Normalized resistivity (ρ_H/ρ_0) as a function of applied low filed at (a) 5 K, (b) 300 K of the LSMO samples.

value at lower temperature without any peak around T_{M-I} (as mentioned in the Introduction), which may be due to the ISPT occurring through the GBs.[3] The MR values up to 1T of sample LSMO-10, LSMO-11 and LSMO-12 reach 22.56, 21.88, 21.63 and 16.54% at 5 K, respectively, which is close to the MR values of similar particle sizes of LSMO materials reported in other articles.[2, 34, 57, 58] However, at 300 K and 1 T, the MR values of the samples are only 4.57, 4.49, 2.36 and 1.30, respectively. Particle size effect has a certain reference value and important reality signification to the enhancement of LFMR values, which is primarily related to the larger GB effect leading to an increase in intergrain exchange interactions and electron polarization.[2, 34, 59] The study of enhanced LFMR effect in the polycrystalline manganites at room temperature for practical application remain to be developed in further research.

4 Conclusions

In summary, our results indicate that particle size effect plays a significant role in determining the electric and magnetic transport properties of the $La_{0.67}Sr_{0.33}MnO_3$ coatings synthesized by sol–gel method. It is displayed that there are different characteristics of nano-sized materials compared with the bulk materials in terms of certain aspects of properties. We emphasize the effect of particle size on the electrical property of the samples in the low temperature region (5 K<T<50 K), ferromagnetic metallic region (50 K<T<Tp) and paramagnetic insulating region (Tp <T<300 K) based on three electrical conduction models. The resistivity minimum at low temperatures is well described by ISPT of electrons through the GBs. It is concluded that decreasing particle sizes leads to the decrease of Tc and Tp, and the enhancement of LFMR, but also results in the reduction of the magnetization and the increase of resistivity. These phenomena are understood as consequences of the increase contribution from the relative effective anisotropy surface and the non-ferromagnetic and insulating intergranular interaction with decreasing particle sizes. Clearly revealed that, the properties can be tuned by varying particle sizes to overcome the conflicting issues and obtain superior performances.

Acknowledgements

This work was financially supported by College Independent Innovation Projects of Jinan City (201202073) and Independent Innovation Projects of Shandong province (2013CXB60201).

References

1 K. Das, B. Satpati and I. Das, *RSC Adv.*, 2015, **5**, 27338-27346.
2 A. Sadhu and S. Bhattacharyya, *Chem. Mater.*, 2014, **26**, 1702-1710.
3 G. Venkataiah, Y. K. Lakshmi, V. Prasad and P. V. Reddy, *J. Nanosci. Nanotechnol.*, 2007, **7**, 2000-2004.
4 C. Zener, *Phys. Rev.*, 1951, **82**, 403-405.
5 A. Tiwari and K. P. Rajeev, *Solid State Commun.*, 1999, **111**, 33-
6 J. B. Goodenough, *Annu. Rev. Mater. Sci.*, 1998, **28**, 1-27.
7 A. Chen, Z. Bi, C. Tsai, L. Chen, Q. Su, X. Zhang and H. Wang, *Cryst. Growth Des.*, 2011, **11**, 5405-5409.
8 S. Ju, H. Sun and Z. Li, *J. Phys.: Condens. Matter*, 2002, **14**, L631-L639.
9 R. Mahendiran, R. Mahesh, A. K. Raychaudhuri and C. N. R. Rao, *Solid State Commun.*, 1996, **99**, 149-152.
10 R. Hiskes, S. DiCarolis, M. R. Beasley, T. H. Geballe and G. J. Snyder, *Phys. Rev. B*, 1996, **53**, 14434-14444.
11 H. A. Reshi, S. Pillai, D. Bhuwal and V. Shelke, *J. Nanosci. Nanotechnol.*, 2013, **13**, 4608-4615.
12 X. W. Cao, J. Fang and K. B. Li, *Solid State Commun.*, 2000, **115**, 201-205.
13 A. Rostamnejadi, H. Salamati and P. Kameli, *J. Supercond. Nov. Magn.*, 2012, **25**, 1123-1132.
14 R. Skomski, *J. Phys.: Condens. Matter*, 2003, **15**, R841.
15 B. Abeles and J. S. Helman, *Phys. Rev. Lett.*, 1976, **37**, 1429-1432.
16 K. Dörr, *J. Phys. D: Appl. Phys.*, 2006, **39**, R125.
17 P. Dey, T. K. Nath, U. Kumar and P. K. Mukhopadhyay, *J. Appl. Phys.*, 2005, **98**, 14306.
18 A. Gupta, G. Gong, G. Xiao, P. Duncombe, P. Lecoeur, P. Trouilloud, Y. Wang, V. Dravid and J. Sun, *Phys. Rev. B*, 1996, **54**, R15629-R15632.
19 J. Wang, B. Gu, H. Sang, G. Ni and Y. Du, *J. Magn. Magn. Mater.*, 2001, **223**, 50-54.
20 N. Gayathri, R. Ranganathan and A. Dutta, *Phys. Rev. B*, 2003, **68**, 54432.
21 A. Banerjee, S. Pal, S. Bhattacharya, B. K. Chaudhuri and H. D. Yang, *J. Appl. Phys.*, 2002, **91**, 5125-5134.
22 L. Joshi and S. Keshri, *Phase Transit.*, 2010, **83**, 263-275.
23 X. Zhu, S. Li, Q. Ao and X. Yang, *Journal of Alloys & Compounds*, 2011, **509**, 7093-7099.
24 Q. Ren, Y. Zhang, Y. Chen, G. Wang, X. Dong and X. Tang, *J. Sol-Gel Sci. Techn.*, 2013, **67**, 170-174.
25 Z. J. Wang, H. Usuki, T. Kumagai and H. Kokawa, *J. Cryst. Growth*, 2006, **293**, 68-73.
26 Z. X. Cheng, H. F. Zhen, A. H. Li, X. L. Wang and H. Kimura, *J. Cryst. Growth*, 2005, **275**, E2415-E2419.
27 J. Yang, B. C. Zhao, R. L. Zhang, Y. Q. Ma, Z. G. Sheng, W. H. Song and Y. P. Sun, *Solid State Commun.*, 2004, **132**, 83-87.
28 G. Venkataiah and P. Venugopal Reddy, *Phase Transit.*, 2009, **82**, 156-166.
29 T. Zhang, G. Li, T. Qian, J. F. Qu, X. Q. Xiang and X. G. Li, *J. Appl. Phys.*, 2006, **100**, 94324.
30 P. Dutta, P. Dey and T. K. Nath, *J. Appl. Phys.*, 2007, **102**, 73906.
31 J. M. Coey, *Phys. Rev. Lett.*, 1971, **27**, 1140-1142.
32 Y. Huang, Z. Xu, C. Yan, Z. Wang, T. Zhu, C. Liao, S. Gao and G. Xu, *Solid State Commun.*, 2000, **114**, 43-47.
33 Y. Tian, D. Chen and X. Jiao, *Chem. Mater.*, 2006, **18**, 6088-6090.
34 V. Dyakonov, A. Ślawska-Waniewska, N. Nedelko, E. Zubov, V. Mikhaylov, K. Piotrowski, A. Szytuła, S. Baran, W. Bazela and Z. Kravchenko, *J. Magn. Magn. Mater.*, 2010, **322**, 3072-3079.
35 P. Kameli, H. Salamati and A. Aezami, *J. Alloy. Compd.*, 2008, **450**, 7-11.
36 A. Asamitsu, Y. Moritomo, H. Kuwahara, Y. Tokura and Y. Tomioka, *Phys. Rev. Lett.*, 1995, **74**, 5108-5111.
37 M. Battabyal and T. K. Dey, *Physica B*, 2005, **367**, 40-47.
38 D. K. Petrov, L. Krusin-Elbaum, J. Z. Sun, C. Feild and P. R. Duncombe, *Appl. Phys. Lett.*, 1999, **75**, 995-997.
39 E. Rozenberg, M. Auslender, I. Felner and G. Gorodetsky, *J. Appl. Phys.*, 2000, **88**, 2578-2582.
40 F. Guinea, A. de Andrés, J. L. Martínez, C. Prieto, L. Vázquez and M. García-Hernández, *Phys. Rev. B*, 2000, **61**, 9549-9552.

41 J. Fontcuberta, B. Martínez, X. Obradors and L. Balcells, *Phys. Rev. B*, 1998, **58**, R14697-R14700.
42 Y. Jin, X. Cui, W. Han, S. Cao, Y. Gao and J. Zhang, *Phys. Chem. Chem. Phys.*, 2015, **17**, 12826-12832.
43 T. K. Nath and P. Dey, *Phys. Rev. B*, 2006, **73**, 214425.
44 J. Fontcuberta, B. Martínez, X. Obradors and L. Balcells, *Phys. Rev. B*, 1998, **58**, R14697-R14700.
45 M. I. Auslender, E. Rozenberg, A. E. Kar Kin, B. K. Chaudhuri and G. Gorodetsky, *J. Alloy. Compd.*, 2001, **326**, 81-84.
46 O. Ciftja, M. Luban, M. Auslender and J. H. Luscombe, *Phys. Rev. B: Condens. Matter Mater. Phys.*, 1999, **60**, 10122.
47 M. Auslender, A. E. Kar Kin, E. Rozenberg and G. Gorodetsky, *J. Appl. Phys.*, 2001, **89**, 6639-6641.
48 G. Venkataiah, D. C. Krishna, M. Vithal, S. S. Rao, S. V. Bhat, V. Prasad, S. V. Subramanyam and P. V. Reddy, *Physica B*, 2005, **357**, 370-379.
49 D. Grossin and J. G. Noudem, *Solid State Sci.*, 2004, **6**, 939-944.
50 V. R. Kumari, G. Venkataiah and P. V. Reddy, *Int. J. Mod. Phys. B*, 2005, **19**, 3619-3629.
51 G. Jakob, F. Martin, W. Westerburg and H. Adrian, *Phys. Rev. B*, 1998, **57**, 10252.
52 S. K. Singh, S. B. Palmer, D. McK. Paul and M. R. Lees, *Appl. Phys. Lett.*, 1996, **69**, 263-265.
53 B. M. Nagabhushana, R. P. Sreekanth Chakradhar, K. P. Ramesh, V. Prasad, C. Shivakumara and G. T. Chandrappa, *J. Alloy. Compd.*, 2008, **450**, 364-368.
54 M. S. Ramachandra Rao, G. Rangarajan, Y. Lu, J. Klein, R. Klingeler, S. Uhlenbruck, B. Büchner, R. Gross and V. Ravindranath, *Phys. Rev. B*, 2001, **63**, 184434.
55 B. Martínez, A. Seffar, S. Piñol, J. L. García-Muñoz, X. Obradors and J. Fontcuberta, 1996, pp. 1122-1125.
56 S. Bhattacharya, R. K. Mukherjee, B. K. Chaudhuri and H. D. Yang, *Appl. Phys. Lett.*, 2003, **82**, 4101-4103.
57 M. A. López-Quintela, L. E. Hueso, J. Rivas and F. Rivadulla, *Nanotechnology*, 2003, 212-219.
58 H. Hwang, S. Cheong, N. Ong and B. Batlogg, *Phys. Rev. Lett.*, 1996, **77**, 2041-2044.
59 P. Vanderbemden, B. Vertruyen, M. Ausloos, B. Rivasmurias and V. Lovchinov, *J. Optoelectron. Adv. Mater.*, 2009, **11**, 1115-1121.